A Theory of Standing Meanders of the Antarctic Circumpolar Current and Their Response to Wind

XIHAN ZHANG,[a,b,c] MAXIM NIKURASHIN,[a,b,c] BEATRIZ PEÑA-MOLINO,[b,e] STEPHEN R. RINTOUL,[b,d,e] AND EDWARD DODDRIDGE[a,b]

[a] *Institute for Marine and Antarctic Studies, University of Tasmania, Hobart, Tasmania, Australia*
[b] *Australian Antarctic Program Partnership, University of Tasmania, Hobart, Tasmania, Australia*
[c] *ARC Centre of Excellence for Climate Extremes, University of New South Wales, Sydney, New South Wales, Australia*
[d] *Centre for Southern Hemisphere Oceans Research, Hobart, Tasmania, Australia*
[e] *CSIRO Oceans and Atmosphere, Hobart, Tasmania, Australia*

(Manuscript received 13 April 2022, in final form 6 September 2022)

ABSTRACT: Standing meanders of the Antarctic Circumpolar Current (ACC) and associated eddy hotspots play an important role for the meridional heat flux and downward momentum transfer in the Southern Ocean. Previous modeling studies show that the vorticity balance characterizing standing meanders in the upper ocean is dominated by advection of relative vorticity and stretching. Through the adjustment of this vorticity balance, standing meanders have been suggested to provide a pathway for the transfer of the momentum input by the wind from the surface to the bottom, leading to stronger bottom flows and energy dissipation. However, the dynamics governing the meander formation and its adjustment to wind remain unclear. Here we develop a quasigeostrophic theory and combine it with a regional model of the Macquarie Ridge region and an idealized channel model to explore the dynamics and vertical structure of standing meanders of the ACC. The results show that the entire vertical structure of the meander, including its dynamics in the upper ocean, is controlled by the bottom flow interacting with topography. Based on our results, we suggest a novel mechanism for the response of the ACC to wind in which "flexing" of the meander, or change in its curvature, is a response to changes in the bottom (barotropic) flow. Stronger bottom flow in response to stronger wind interacts with topography and generates a larger-amplitude Rossby wave propagating into the upper ocean. The ACC mean shear aloft amplifies the Rossby wave and leads to a larger-amplitude meander in the upper ocean dominated by advection of relative vorticity and stretching.

KEYWORDS: Southern Ocean; Barotropic flows; Bottom currents; Ocean dynamics; Rossby waves; Topographic effects

1. Introduction

A well-known feature of the Antarctic Circumpolar Current (ACC) is the relative insensitivity of its total transport to changes in the wind (e.g., Rintoul and Garabato 2013). The canonical understanding of the equilibration of the ACC and its response to the wind is from a zonally averaged perspective, in which the eddy-induced overturning circulation directly opposes the wind-driven overturning circulation (e.g., Marshall and Radko 2003). In this framework, changes in the wind-driven circulation are thought to be compensated by changes in the eddy-induced circulation leading to the insensitivity of isopycnal slopes in the ocean interior, and hence of the baroclinic transport of the ACC to wind (e.g., Hallberg and Gnanadesikan 2006; Meredith and Hogg 2006; Marshall and Speer 2012; Munday et al. 2013; Farneti et al. 2015; Marshall et al. 2017). However, the eddy activity and corresponding meridional eddy heat fluxes are known to be heterogeneous along the path of the ACC, with strong enhancement in standing meanders (e.g., Williams et al. 2007; Thompson and Naveira Garabato 2014; Farneti et al. 2015).

Modeling studies have recently highlighted the important role of standing meanders for the equilibration of the ACC and its response to wind. Thompson and Naveira Garabato (2014, hereafter TNG14), propose a mechanism in which increased wind stress at the surface leads to "flexing" of the ACC meanders—that is, changes in meander curvature—resulting in efficient downward transfer of momentum input from the surface, where momentum is supplied by the wind, to the bottom, where wind stress is balanced by bottom form stress. Using an idealized model of the Southern Ocean, Abernathey and Cessi (2014) explore the interplay between standing meanders and transient eddies and suggest that the standing meanders amplify the effect of transient eddies by increasing the local buoyancy gradients (or stretching buoyancy contours), increasing the efficiency of heat transport by transient eddies. Likewise, using regional models of the Southern Ocean, Dufour et al. (2012) show that as winds increase, standing meanders become the main contributor to balancing the wind-driven overturning circulation. The role of the ACC barotropic dynamics and its interaction with topography for controlling the ACC transport has also been recently highlighted in Masich et al. (2015), Constantinou and Young (2017), Constantinou (2018), and Constantinou and Hogg (2019).

The dynamics of standing meanders is traditionally understood in the context of Rossby wave theory (e.g., Hughes 2005). The interaction between the ACC flow and large-scale midocean ridges leads to topographically generated Rossby

Corresponding author: Xihan Zhang, xihan.zhang@utas.edu.au

DOI: 10.1175/JPO-D-22-0086.1

waves. Rossby waves propagate westward against the mean flow in the ACC, and a stationary Rossby wave can form when the westward phase speed of the wave matches the eastward speed of the mean flow. The superposition of a stationary Rossby wave and the ACC mean flow forms a standing meander in the ACC. The quasigeostrophic Rossby wave dispersion relation indicates that the dominant vorticity balance for short Rossby waves is between advection of planetary vorticity and advection of relative vorticity, while, for long Rossby waves, it is between advection of planetary vorticity and the stretching (or divergence) term. Comparing maps of vorticity budget terms derived from satellite altimetry, Hughes (2005) finds that the surface vorticity balance of the Southern Ocean is consistent with the short Rossby wave dynamics, showing a balance between advection of planetary vorticity and advection of relative vorticity. The characteristic spatial scales in the vorticity terms were found to be around 300–500 km. These scales correspond to short barotropic Rossby waves, implying that the meanders have a predominantly barotropic structure. A similar vorticity balance was obtained from lowered acoustic Doppler current profilers in the subantarctic front upstream of Drake Passage (Chereskin et al. 2010).

In contrast, TNG14 find that the dominant vorticity balance at 250-m depth within ACC meanders is between the advection of relative vorticity and stretching, with the advection of planetary vorticity being one order of magnitude smaller, based on analysis of an eddy-resolving ocean model. TNG14 suggest that the discrepancy between the model and altimetry results can be attributed to the smoothing filter applied to the altimetry: smoothing results in a larger dominant scale of the relative vorticity advection, a scale at which it is balanced by the advection of planetary vorticity. In the TNG14 model, the leading terms in the vorticity balance (advection of relative vorticity and stretching) are highly correlated with bottom speed within the meander (TNG14). Based on this correlation, the authors propose a mechanism to explain the insensitivity of the ACC to wind: changes in wind drive changes in meander curvature, which alters terms in the vorticity balance and results in downward momentum transfer, an increase in the bottom speed, and energy dissipation. By invoking downward momentum transfer within the meander, TNG14 imply that flexing of a standing meander in the upper ocean leads to changes in the bottom flow—a mechanism that we refer to as a "top-down" control below. However, the mechanism proposed by TNG14 has not been tested with models or observations.

In this study, we develop a quasigeostrophic (QG) Rossby wave theory to investigate the formation and vertical structure of standing meanders in the ACC. We test the theory with a high-resolution regional ocean model of a prominent ACC meander upstream of the Macquarie Ridge, and a suite of idealized simulations of wind-driven flow over a ridge. The models show that the dominant upper-ocean vorticity balance within the meander is between the advection of relative vorticity and stretching, consistent with TNG14. A simple QG theory explains that the entire meander, including the dominant terms in the upper-ocean vorticity balance, is maintained by the bottom flow interacting with topography. The resulting vorticity balance has two regimes. In the deep ocean, advection of planetary vorticity plays a leading role. In the upper ocean, the vertical shear of the ACC mean flow amplifies the bottom generated Rossby wave signal. This results in a regime transition within the water column and leads to the dominance of the advection of relative vorticity in the upper ocean. We also explore the sensitivity of the meander to wind changes and show that it is the bottom (barotropic) flow component that drives the ACC meander response to changes in wind forcing. This implies a "bottom-up" control mechanism, in which changes in the bottom flow lead to flexing of standing meanders in the upper ocean. This is in contrast to the top-down control mechanism proposed by TNG14.

The paper is structured as follows. In section 2, we present our modeling results. We describe the configuration of the regional model of the Southern Ocean sector south of Tasmania and New Zealand and configuration of the idealized model. Then, we discuss both the horizontal and vertical distribution of the vorticity balance terms. In section 3, we present the formulation of the QG theory and show how the theory explains the vertical structure of ACC meanders and the dominance of advection of relative vorticity and stretching in the upper ocean. The sensitivity of ACC meanders to changes in wind forcing is discussed in section 4, based on the QG theory and model simulations. Finally, we summarize and discuss the implications of the results in section 5.

2 Model simulations of ACC meanders

In this study, we use a combination of two numerical models and theory to investigate the dynamics of standing meanders in the ACC and their sensitivity to wind. We use a *regional* model to simulate the ocean circulation in realistic ocean conditions, including realistic topography, and open boundary and surface forcing. This regional model configuration motivates our study and allows us to compare our results to previous ocean models (e.g., TNG14). To develop further insight into the dynamics of ACC meanders, we also use an *idealized* periodic channel model of the Southern Ocean with a ridge. The idealized model allows us to carry out a parameter sensitivity study and explore the response of the meander to a wide range of wind stress amplitudes.

a. Regional model configuration

Our regional model focuses on one of the major standing meanders in the Southern Ocean formed downstream of the Southeast Indian Ridge (TNG14; Zhang and Nikurashin 2020). A hydrostatic primitive equation Massachusetts Institute of Technology general circulation model (MITgcm) (Marshall et al. 1997) is configured to simulate the region south of Tasmania and New Zealand including both the Southeast Indian Ridge and the Macquarie Ridge (135°–165°E, 48°–60°E). The horizontal resolution of the model is 1/20° (around 3 km) and it has 200 vertical levels varying from 4 m at the surface to 40 m at depth. At this resolution, mesoscale and submesoscale eddies and abyssal hills on O(10–100) km scale are well resolved both horizontally and vertically. High-resolution

bathymetry from the Shuttle Radar Topography Mission (SRTM30_PLUS) (Becker et al. 2009; Sandwell and Smith 2009) is used in this model. Open boundary conditions are monthly mean temperature, salinity and velocity fields taken from a 1/10° global ocean model ACCESS-OM2-01 forced by the 1984–85 repeat-year JRA-55 driving ocean (JRA55-do), version 1.3, atmospheric forcing (http://cosima.org.au; Kiss et al. 2020). No-slip boundary conditions are applied at the bottom and side boundaries. Two-degree-wide sponge layers are used at the open boundaries with a restoring time scale changing from 1 month in the interior to 1 day at the boundary. At the surface, the simulation is driven by the monthly averaged wind stress from ACCESS-OM2-01 and restoring to monthly averaged surface temperature and salinity fields from ACCESS-OM2-01 with a 10-day restoring time scale. The model is run for 4 years for the analysis following a period of model spinup and equilibration. Ten-day averaged, online momentum term diagnostics are saved and used to estimate vorticity balance terms. For a more detailed discussion of the model configuration and model validation, the reader is referred to Zhang and Nikurashin (2020), who used a similar regional model configuration.

b. *Idealized model configuration*

As for the regional model, the idealized model is also based on the MITgcm. The model is similar to previous channel models of the Southern Ocean and, specifically, follows the configuration used in Abernathey et al. (2011). The model has a 2000 km × 2000 km zonally periodic domain with a 3-km depth. The horizontal resolution is 10 km. There are 40 vertical levels with varying resolution ranging from 10 m at the surface to 233 m at the bottom. At this resolution, the model does not resolve submesoscale motions and thus allows us to focus on large-scale meander dynamics. A 1-km-tall, Gaussian meridional ridge extending across the entire channel is placed in the middle of the domain, similar to the simulation with topography in Abernathey and Cessi (2014). At the surface, steady idealized (sinusoidal) zonal wind stress with 0.1 N m^{-2} peak amplitude and heat flux profiles are prescribed. At the northern boundary, there is a 100-km-wide sponge layer within which an exponential vertical temperature profile is maintained. Parameters and forcing profiles used in the model are identical to those in Abernathey et al. (2011). Online diagnostics of momentum equation terms are saved as annual means for the computation of the vorticity budget terms. In the parameter sensitivity study, the surface wind stress amplitude is perturbed to explore the meander sensitivity to wind. In addition to the wind stress used in the reference simulation, half wind, double wind and triple wind experiments are also conducted. The reference simulation is run for 100 years to equilibrium. The reference simulation and each of the perturbation experiments are then run for additional 30 years to steady state.

c. *Regional bathymetry and circulation*

This region is part of the Macquarie Fault Zone, which is characterized by a range of scales and seafloor features. The Macquarie Ridge is located in the eastern part of the region at around 160°E (Fig. 1a). The ridge is very narrow (width of 80 km) and tall (height up to 5 km) extending across several degrees from 50°S to around 56°S. The Southeast Indian Ridge is located in the western part of the region upstream of the Macquarie Ridge. It is oriented in the northwest–southeast direction and is relatively short (height of about 1 km) and wide (width of 500 km). Between the two midocean ridges, there is a relatively flat abyssal plane with an average depth of around 4000 m. In addition to the large-scale topographic features, the region also contains small-scale features such as small ridges, sea mounts, and abyssal hills.

The regional circulation is illustrated by snapshots of the sea surface temperature and ocean currents in Fig. 1b. The large-scale circulation is dominated by the ACC fronts: the Subantarctic Front (SAF) between 52° and 54°S and the Polar Front (PF) south of 54°S [approximately corresponding to sea surface height (SSH) contours from −0.5 to 0 m and from 0.1 to 0.5 m shown in Fig. 1c, respectively]. The fronts meander as they are steered north by the Southeast Indian Ridge and then flow eastward across the region. The prominent standing meander in this region is illustrated by the time-mean sea surface height contours in Fig. 1c. The meander forms in the region downstream of the Southeast Indian Ridge and upstream of the Macquarie Ridge. Consistent with previous studies (e.g., TNG14), eddy activity is enhanced within the meander region as shown by the time-mean eddy kinetic energy in Fig. 1c. Vigorous eddies can be clearly seen in the sea surface temperature distribution (Fig. 1b), especially within the meander directly upstream of the Macquarie Ridge.

d. *Vorticity balance within the meander region*

Previous studies (e.g., Hughes 2005; Chereskin et al. 2010) of the vorticity balance of standing meanders in the ACC have mostly focused on the horizontal distribution of the vorticity terms. In this study, we also consider the vertical distribution of vorticity terms to explore how flow over topography influences the vorticity balance.

Following TNG14, we consider a steady QG flow approximation. The QG vorticity balance in the interior (e.g., Gill 1982) is given by

$$\mathbf{u} \cdot \nabla\zeta + \beta v - f\,\frac{\partial w}{\partial z} = 0, \tag{1}$$

where $\mathbf{u} = (u, v)$ is the horizontal velocity vector, $\zeta = v_x - u_y$ is the relative vorticity, $f = f_0 + \beta y$ is the planetary vorticity, f_0 is a constant Coriolis parameter, β is the planetary vorticity gradient, and $\partial w/\partial z$ is the vertical velocity gradient representing horizontal flow divergence. Terms of the vorticity balance from left to right are the advection of relative vorticity, advection of planetary vorticity, and stretching of the water column due to horizontal flow divergence. The full vorticity budget, including tendency, wind stress, and frictional terms, is calculated from the model outputs by applying a curl operator to all momentum term diagnostics computed online. We find that the full budget is well closed with a residual three orders of magnitude smaller than the vorticity tendency, the smallest

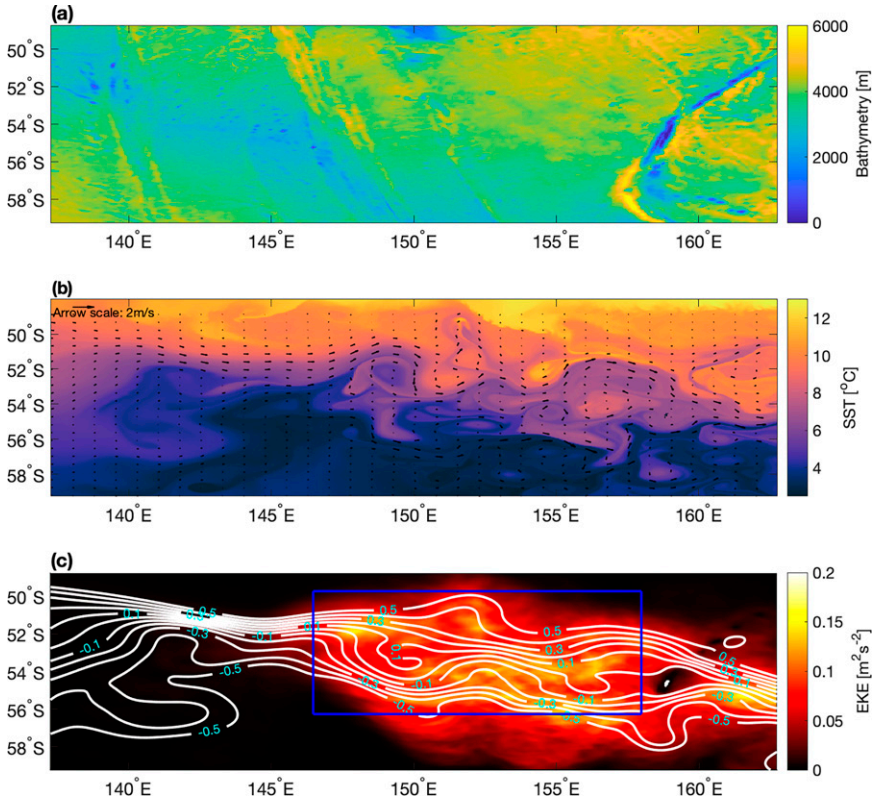

FIG. 1. (a) Bathymetry (m), (b) snapshot of sea surface temperature (°C) with velocity vectors (m s^{-1}) superimposed, and (c) 4-yr averaged eddy kinetic energy (m^2 s^{-2}) and sea surface height (m) in the regional model. The meander region is shown in the blue box.

term in the budget. Given that the focus of this study is on the large-scale meander, which is well approximated by the QG dynamics, only the terms in (1) accounting for 90% of the budget for the meander in the upper ocean are presented and discussed below.

We first examine the distribution of the terms in the QG vorticity balance in (1) in the regional model. Maps of the time-averaged vorticity balance terms at 250 m are shown in Fig. 2. Vorticity balance in the upper ocean is dominated by the advection of relative vorticity and stretching terms, with the advection of planetary vorticity being an order of magnitude smaller. Advection of relative vorticity and stretching are spatially anticorrelated. All three terms show a large-scale meander signal with a 200–400-km horizontal scale and alternating positive and negative values corresponding to the crests and troughs of the meander. In addition, advection of relative vorticity and stretching show small-scale features on 10–100-km scales superimposed on the large-scale meander signal. The small-scale features are not present in the advection of planetary vorticity map. The distribution and magnitudes of vorticity terms are consistent with TNG14.

In addition to the horizontal distribution, we also examine the vertical structure of vorticity balance terms at 54°S, approximately through the center of the meander (Fig. 3). The balance between advection of relative vorticity and stretching holds throughout the water column, but the dominant spatial scale varies with depth. The small-scale signal in the deep ocean is greater in magnitude than the upper-ocean signal and decays away from topography in the bottom 1 km. The small-scale signal in the deep ocean is also not present in the advection of planetary vorticity. The advection of planetary vorticity is dominated by large-scale features and has a relatively barotropic vertical structure with some surface intensification.

The corresponding results from the idealized model are shown in Fig. 4. A ridge in the middle of the domain generates a single standing meander downstream of the ridge. As in the regional model, vorticity balance in the idealized model is dominated by the advection of relative vorticity and stretching in the upper ocean (Figs. 4b,c). The scales and amplitudes are similar to those in the regional model. However, small-scale features seen in the deep ocean in the regional model are absent in the idealized simulation. There is no small-scale topography in this simulation and hence the horizontal scale of the flow response is set by the horizontal scale of the ridge.

In summary, the regional and idealized model results show that the distribution of the vorticity balance terms is consistent with previous modeling studies and shows that advection of relative vorticity balances stretching both at small and large scales, and in the deep and upper ocean. In the following

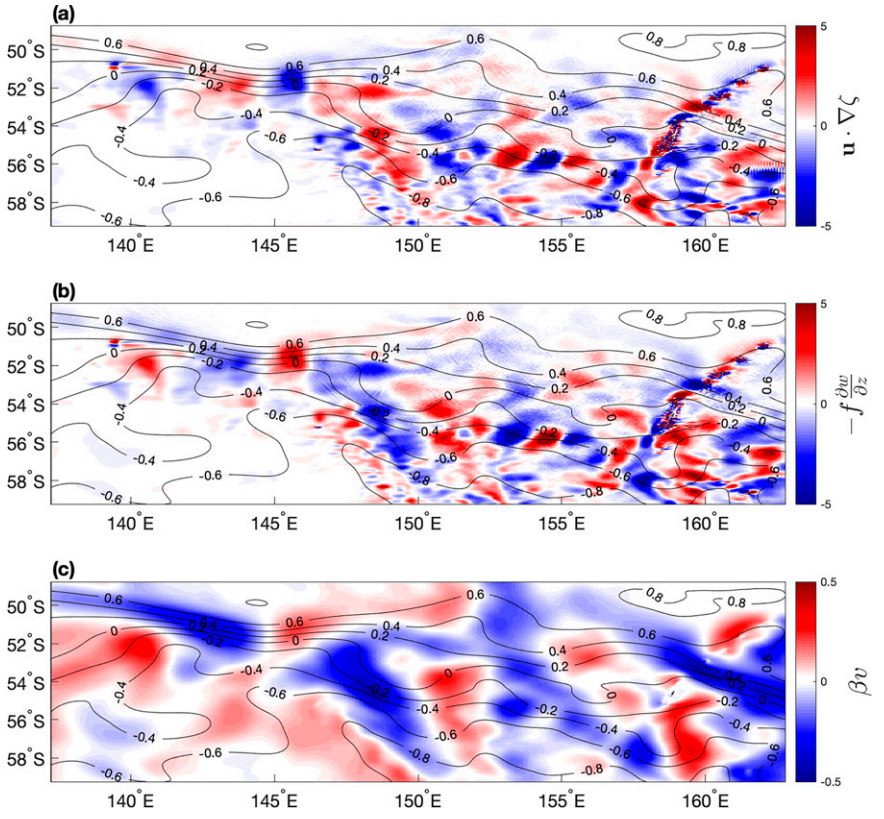

FIG. 2. The 4-yr averaged vorticity terms (10^{-11} s^{-2}) at 250-m depth superimposed with time-mean sea surface height contours (m) in the regional model: (a) advection of relative vorticity $\mathbf{u} \cdot \nabla \zeta$, (b) stretching (horizontal divergence) $-f(\partial w/\partial z)$, and (c) advection of planetary vorticity βv. The color scale in advection of planetary vorticity is a factor of 10 smaller than those in the other two terms.

section, we use QG theory to explain the vorticity balance distribution seen in the models and its relation to Rossby wave dynamics. In particular, we explain the different spatial scales in the upper and deep ocean and show that the upper-ocean meander vorticity balance is set by the interaction between the bottom flow and topography, not by the surface flow as proposed in previous studies.

3. A theory of the meander

To explore the underlying dynamics of standing meanders in the ACC and their response to changes in the wind, we develop a simple theoretical model of a stratified QG flow over topography. We show that the meander vertical structure and its vorticity balance in the upper ocean result from a regime change within the water column caused by the strong vertical shear of the mean flow. In this section, we first formulate the QG theory and discuss the assumptions made. Then we show that uniform mean flow over small- and large-scale topography leads to different vorticity balance regimes. Finally, we extend the problem to a vertically sheared mean flow over large-scale topography to explore how the two regimes interact to determine the vertical structure of the ACC meander vorticity terms.

a. *Theory formulation*

The governing QG potential vorticity (QGPV) equation (e.g., Salmon 1998; Vallis 2019) is

$$\frac{\partial q}{\partial t} + \mathbf{u} \cdot \nabla q = 0, \tag{2}$$

where the QGPV, q, can be written as

$$q = \nabla^2 \psi + f + \frac{\partial}{\partial z}\left(\frac{f_0^2}{N^2}\frac{\partial \psi}{\partial z}\right), \tag{3}$$

where ψ is the streamfunction, from which the flow is derived ($u = -\partial\psi/\partial y$ and $v = \partial\psi/\partial x$), and $N(z)$ is the stratification. The terms in the QGPV from left to right are relative vorticity, planetary vorticity, and stretching. The steady state of (2) corresponds to the vorticity balance in (1) diagnosed from the models.

We look for solutions in the form $\psi = \overline{\psi} + \psi'$, where $\overline{\psi}$ represents a prescribed mean flow and ψ' represents perturbations, defined as deviations from the mean. We assume that the perturbations are small and thus the governing equation can be linearized. We consider a zonal mean flow that varies with depth, that is, $\overline{\mathbf{u}} = [\overline{u}(z), 0]$, and also assume a steady

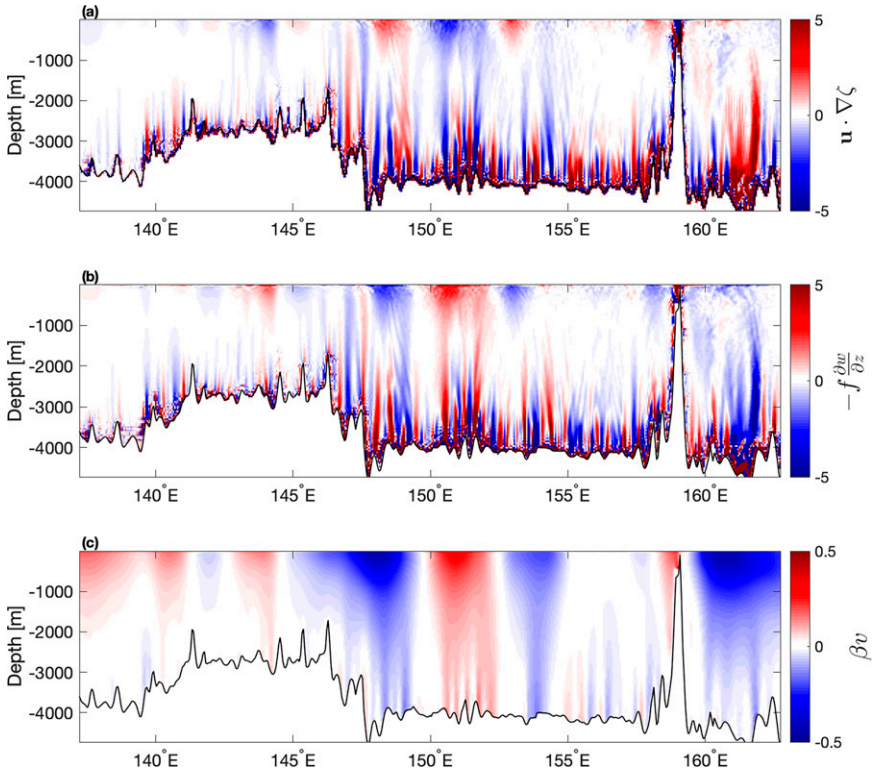

FIG. 3. Vertical sections of time-averaged vorticity terms (10^{-11} s^{-2}) at 54°S in the regional model: (a) advection of relative vorticity $\mathbf{u} \cdot \nabla\zeta$, (b) stretching (horizontal divergence) $-f(\partial w/\partial z)$, and (c) advection of planetary vorticity βv. The color scale in advection of planetary vorticity is a factor of 10 smaller than those in the other two terms.

state such that both the mean flow and perturbations are constant in time, that is, we look for a standing solution. Applying these assumptions and the flow decomposition, the governing equation for perturbations becomes

$$\overline{u}\,\frac{\partial}{\partial x}\left[\nabla^2\psi' + \frac{\partial}{\partial z}\left(\frac{f_0^2}{N^2}\,\frac{\partial\psi'}{\partial z}\right)\right] + \left[\beta - \frac{\partial}{\partial z}\left(\frac{f_0^2}{N^2}\,\frac{\partial\overline{u}}{\partial z}\right)\right]\frac{\partial\psi'}{\partial x} = 0. \tag{4}$$

For algebraic simplicity, we further assume that stratification N is constant and that the mean flow shear is weak, that is

$$\frac{\partial}{\partial z}\left(\frac{f_0^2}{N^2}\,\frac{\partial\overline{u}}{\partial z}\right) \ll \beta, \tag{5}$$

so that its contribution to the mean potential vorticity gradient can be neglected. This assumption is justified for weak mean ACC shear in the deep ocean or idealized linear and constant mean flow profiles. In case of a realistic mean ACC flow profile, however, this term is significant and responsible for baroclinic instability and the formation of eddies in the upper ocean, which are expected to act on the meander formation dynamics described in this study. We also consider stratified mean flow over a one-dimensional (1D) sinusoidal topography given by

$$h(x) = h_0 \cos(kx), \tag{6}$$

where h_0 is the amplitude of topography and k is its horizontal wavenumber. The 1D topography implies that the solution has no gradients in the meridional direction. These additional assumptions allow for significant simplifications of the governing equation and are also appropriate for the Southern Ocean. Making these simplifications and looking for solutions in the plane wave form,

$$\psi' = \phi(z)e^{ikx}, \tag{7}$$

where $\phi(z)$ is an unknown vertical structure of the real part of the solution, the governing QG potential vorticity equation reduces to

$$\frac{d^2\phi}{dz^2} + \Lambda^2\phi = 0, \tag{8}$$

where

$$\Lambda^2 = \frac{N^2}{f_0^2}\left(\frac{\beta}{\overline{u}} - k^2\right). \tag{9}$$

Parameter Λ is the only governing parameter of the problem and it captures the relative importance of the mean flow and the horizontal scale of bottom topography in influencing the flow response.

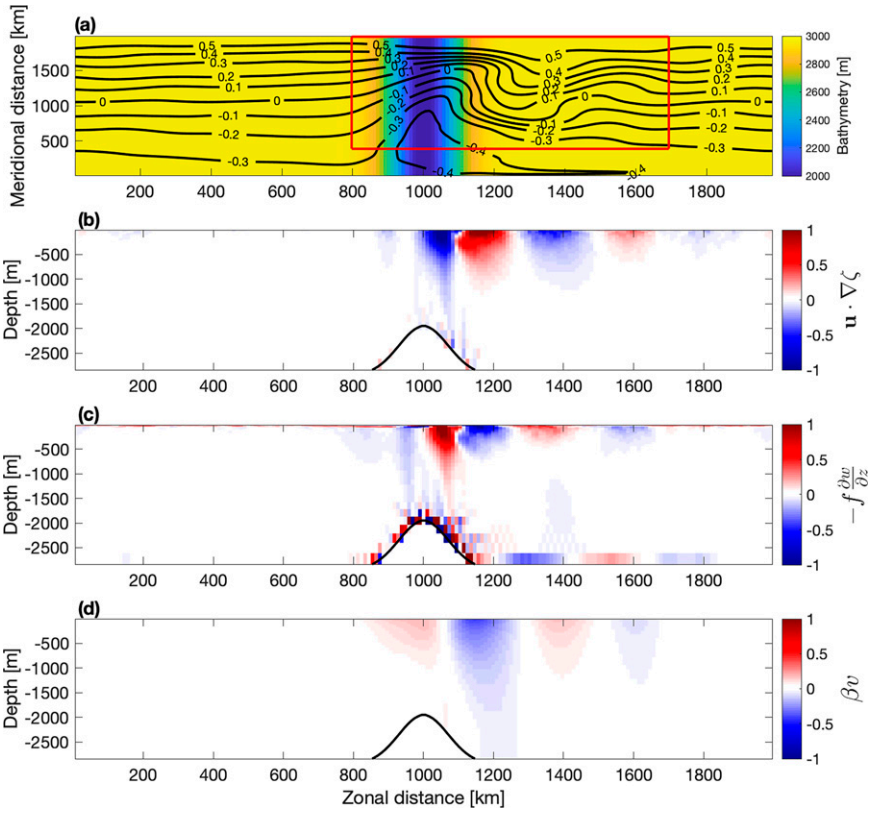

FIG. 4. (a) Bathymetry (m) and time-mean sea surface height (m). Vorticity terms along a section at $y = 1200$ km in the idealized model with reference wind stress (10^{-11} s^{-2}): (b) advection of relative vorticity $\mathbf{u} \cdot \nabla\zeta$, (c) stretching (horizontal divergence) $-f(\partial w/\partial z)$, and (d) advection of planetary vorticity βv.

To solve the governing Eq. (8), the top and bottom boundary conditions are needed. We use the conventional boundary condition of zero vertical velocity of perturbations w' at the surface ($z = 0$) and a linearized no-flow across the boundary condition at the bottom ($z = -H$), that is,

$$w' = 0, \quad \text{at } z = 0, \quad \text{and} \tag{10}$$

$$w' = \overline{u} h_x, \quad \text{at } z = -H, \tag{11}$$

where H is the ocean depth.

In QG theory the vertical velocity can be expressed as a function of the streamfunction, $w' = -f_0/N^2 \overline{u} \psi'_{xz}$, derived using the buoyancy equation (not shown) (e.g., Vallis 2019). Applying the plane wave solution in (7), the boundary conditions for the vertical structure become

$$\phi_z = 0, \quad \text{at } z = 0, \quad \text{and} \tag{12}$$

$$\phi_z = -\frac{N^2}{f_0} h_0, \quad \text{at } z = -H. \tag{13}$$

The governing equation in (8) combined with the boundary conditions in (12) and (13) represents a boundary value problem for a stationary Rossby wave generated by mean flow over bottom topography. It is a simple second-order differential equation that describes the vertical structure of a standing perturbation (wave) in a nonuniform flow. The sign of the parameter Λ^2 gives rise to two distinct regimes of the flow response to topography, as discussed in detail below. Once the solution to the governing equation is found (and only the real part of the solution is taken), the corresponding vorticity balance terms in (1) can be reconstructed as follows

$$\beta v = \beta \psi'_x = -k\beta\phi \sin(kx), \tag{14}$$

$$\mathbf{u} \cdot \nabla\zeta = -k^2 \overline{u} \psi'_x = k^3 \overline{u} \phi \sin(kx), \quad \text{and} \tag{15}$$

$$f\frac{\partial w}{\partial z} = -\frac{f_0^2}{N^2} \overline{u} \psi'_{xzz} = k\frac{f_0^2}{N^2} \overline{u} \phi_{zz} \sin(kx). \tag{16}$$

In Eqs. (14)–(16), the horizontal structure of the perturbations and all of the corresponding vorticity balance terms is set by the horizontal structure of the topography. The vertical structure is given by the solution to the boundary value problem $\phi(z)$. In addition, the vertical structure of the advection of relative vorticity and stretching terms (but not of the advection of planetary vorticity) is scaled by the mean flow vertical structure $\overline{u}(z)$.

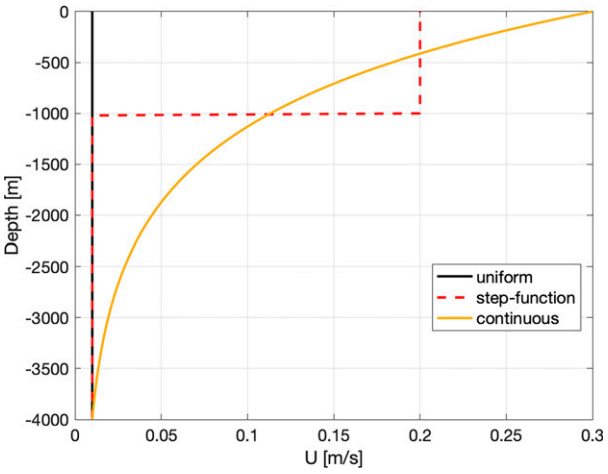

FIG. 5. Velocity profiles (m s^{-1}) used in the quasigeostrophic model.

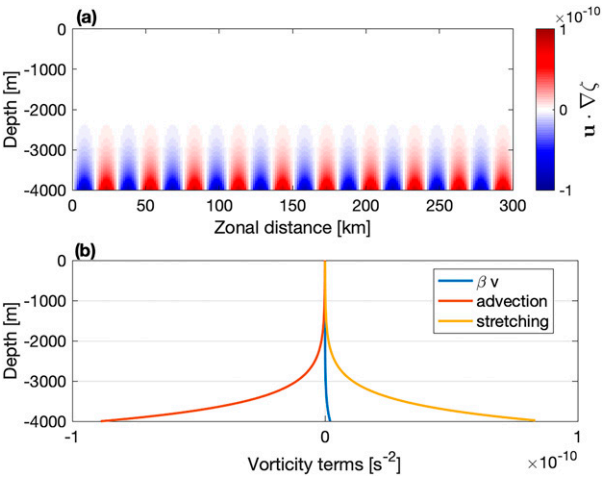

FIG. 6. Vorticity terms (s^{-2}) from the quasigeostrophic model for small-scale topography limit: (a) vertical section of advection of relative vorticity term, and (b) vertical structure of all vorticity terms including advection of relative vorticity $\mathbf{u} \cdot \nabla\zeta$, stretching $-f(\partial w/\partial z)$, and advection of planetary vorticity βv.

b. *Small-scale topography and uniform mean flow limit*

We first consider a uniform mean flow interacting with small-scale topography. We argue that this interaction drives the small-scale vorticity balance response dominating the deep ocean shown in Fig. 3. For characteristic horizontal scale and amplitude of the small-scale topography we choose 30 km, that is, the topographic wavenumber of $k = 2.1 \times 10^{-4}$ m^{-1}, and $h_0 = 200$ m, representative of sea mounts and abyssal hills. For a typical time-mean, large-scale Southern Ocean bottom flow of 1 cm s^{-1} (Fig. 5) and $\beta = 10^{-11}$ m^{-1} s^{-1} we find that $\beta \ll k^2\overline{u}$, and hence

$$\Lambda^2 \approx -\frac{N^2}{f_0^2}\, k^2. \tag{17}$$

Parameter Λ^2 is negative in this limit and corresponds to a topographically trapped (or evanescent) wave regime. In the limit of $\beta \ll k^2\overline{u}$, the advection of planetary vorticity is expected to play a minor role in the governing QG dynamics, and hence in the vorticity balance in (1): the dominant vorticity terms are the advection of relative vorticity and stretching. A full analytical solution to the governing Eq. (8) satisfying boundary conditions in (12) and (13) for the vertical structure of perturbations is

$$\phi(z) = \frac{N^2 h_0}{f_0 \Lambda_i}\, \frac{\cosh(\Lambda_i z)}{\sinh(\Lambda_i H)} \tag{18}$$

where

$$\Lambda_i = \frac{N}{|f_0|} k \tag{19}$$

is the imaginary part of Λ.

In this regime, the perturbation generated by the mean flow over small-scale topography decays exponentially away from topography with the vertical decay (*e*-folding) scale given by Λ_i^{-1}. Using typical values for the Southern Ocean stratification of $N = 10^{-3}$ s^{-1} and Coriolis parameter of $f_0 = -10^{-4}$ s^{-1}, we find that the decay scale is about 500 m. This scale is in a good agreement with the vertical scale of the dominant small-scale signal in the deep ocean shown in Fig. 3. The mean ACC flow is more or less vertically uniform over the bottom 500–1000 m and hence the uniform mean flow assumption used here is appropriate for the flow response to small-scale topography.

The horizontal and vertical distribution of the vorticity terms of the analytical solution estimated using (14)–(16) are shown in Fig. 6. We can see that the advection of planetary vorticity is indeed negligible compared to the advection of relative vorticity and stretching. The advection of relative vorticity and stretching decay away from topography and are anticorrelated, consistent with the model results in Fig. 3. The solution in this limit describes a nonradiating response of stratified rotating flow to a topographic bump—that is, a stratified Taylor column (Johnson 1977). The vertical extent of the perturbation is a result of a competition between rotation and stratification acting to couple and decouple flows in the vertical, respectively. In the limit of decreasing stratification or increasing rotation, the vertical scale Λ_i^{-1} increases, leading ultimately to a barotropic (i.e., infinite vertical scale) Taylor column response to topography. The amplitude of the perturbation in (18) is independent of the mean flow $\overline{u}$. This is a result of the vertical scale of the perturbation being independent of the mean flow, and both the advection of relative vorticity and stretching scaling linearly with the mean flow velocity $\overline{u}$ as seen in (15) and (16). If the mean flow $\overline{u}$ increases, the bottom topography will induce a stronger vertical velocity, which in turn will lead to stronger stretching of the water column above topography. The opposite happens if the mean flow decreases. The advection of relative vorticity will vary at the same rate with $\overline{u}$ and hence will compensate for changes in the stretching term

without changes in the vertical structure of the perturbation $\phi(z)$.

c. Large-scale topography and uniform mean flow limit

We now consider a uniform mean flow interacting with large-scale topography, such as the Southeast Indian Ridge in our regional model domain, which is expected to lead to the formation of a standing meander. We choose a characteristic horizontal scale and amplitude of a large-scale topography of 500 km, corresponding to $k = 1.3 \times 10^{-5}$ m^{-1}, and $h_0 = 1000$ m, respectively. Using 1 cm s^{-1} mean flow magnitude as before, we find that $\beta \gg k^2\overline{u}$, leading to

$$\Lambda^2 \approx \frac{N^2\beta}{f_0^2\overline{u}}. \tag{20}$$

The Λ^2 is positive in this limit, corresponding to the wave radiating regime. The solution to the governing Eq. (8) satisfying the surface and bottom boundary conditions in this limit is

$$\phi(z) = -\frac{N^2 h_0}{f_0|\Lambda|}\frac{\cos(\Lambda z)}{\sin(\Lambda H)}, \tag{21}$$

where

$$\Lambda = \frac{N}{|f_0|}\left(\frac{\beta}{\overline{u}}\right)^{1/2} \tag{22}$$

is the vertical wavenumber of a standing Rossby wave. In this regime, the interaction between the bottom flow and large-scale topography leads to the generation of a stationary Rossby wave with a vertical wavelength given by $2\pi\Lambda^{-1}$. Using typical Southern Ocean parameter values as above, we find that the vertical wavelength is around 20 km. This scale is greater than the depth of the ocean, 4 km, and hence the Rossby wave vertical structure varies little over the ocean depth. The horizontal wavenumber of the solution is fixed by the wavenumber of topography in our problem. In contrast, the vertical wavenumber in (22) can adjust to changes in the mean flow $\overline{u}$ to select the stationary Rossby wave that gets arrested by the mean flow.

The horizontal and vertical distribution of the analytical vorticity terms are shown in Fig. 7. As opposed to the small-scale topography limit, the advection of planetary vorticity dominates the vorticity balance in the large-scale topography limit with the other two terms adding up to balance it. Given that $\Lambda H \ll 1$, we can use the corresponding Taylor expansions to further simplify (21) to the following

$$\phi(z) \approx -\frac{f_0 h_0 \overline{u}}{\beta H}\cos(\Lambda z). \tag{23}$$

According to Eq. (23), the amplitude of a stationary Rossby wave, and hence of the meander formed by a superposition of the stationary Rossby wave and the mean flow, scales linearly with the mean flow $\overline{u}$. As in the small-scale topography limit above, stronger mean flow leads to stronger stretching/squashing of the water column above topography. However, in this limit, the stretching induced by topography is balanced by changes in the advection of planetary vorticity, leading therefore to a larger meridional velocity and hence larger amplitude of Rossby wave and meander. The opposite happens for a weaker mean flow.

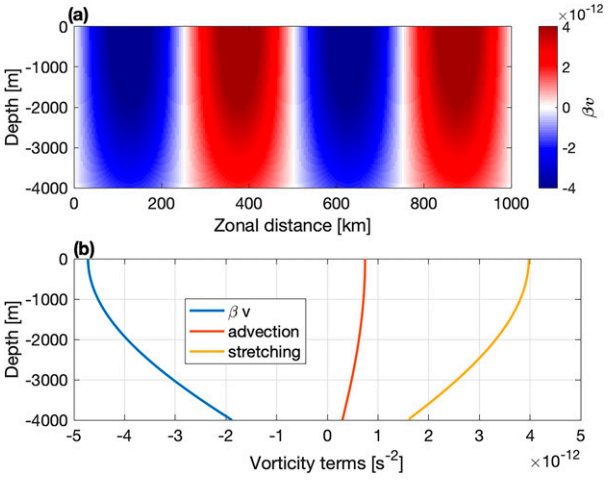

FIG. 7. Vorticity terms (s^{-2}) from the quasigeostrophic model for large-scale topography limit: (a) vertical section of advection of planetary vorticity term and (b) vertical structure of all vorticity terms including advection of relative vorticity $\mathbf{u} \cdot \nabla\zeta$, stretching $-f(\partial w/\partial z)$, and advection of planetary vorticity βv.

While the QG theory solution for a uniform mean flow over large-scale topography describes the generation of a standing Rossby wave, the vertical structure of the solution and terms in the vorticity balance are inconsistent with the vertical structure seen in the regional and idealized models (Figs. 3, 4). With the exception of vorticity terms associated with the small-scale topography present in the regional model (but not in the idealized model), large-scale vorticity balance terms are surface intensified and the advection of planetary vorticity plays a minor role in the upper ocean in the models. Moreover, with the ACC mean flow increasing by an order of magnitude in the upper ocean, the assumption of uniform mean flow made here is not justified for a full-depth Rossby wave. Next, we relax this assumption and explore the generation of stationary Rossby waves by a vertically sheared mean flow.

d. Vertically sheared mean flow

In this section, we consider a vertically sheared mean flow interacting with large-scale topography. The governing equation in (8) cannot be solved analytically for an arbitrary mean flow vertical profile $\overline{u}(z)$. Below, we first solve the governing QG equation numerically for a continuously sheared mean flow profile representative of the ACC flow. Then, we consider a step function change in the mean flow profile as a simple representation of sheared flow and solve the problem analytically to obtain theoretical scalings for the meander structure and amplitude in terms of the problem parameters. We use the same typical parameter values as in previous sections, and again focus on large-scale topography, $k = 1.3 \times 10^{-5}$ m^{-1}, to explore how

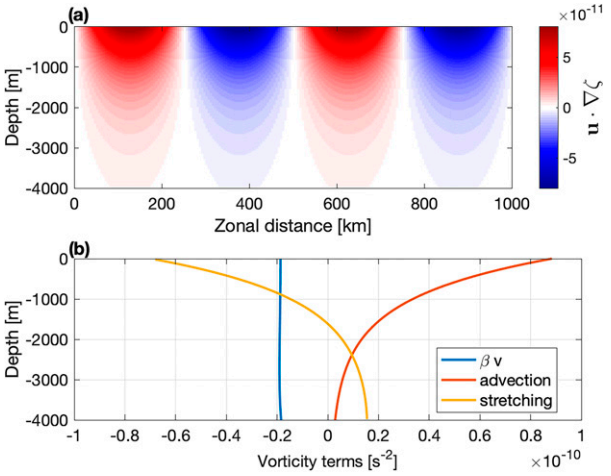

FIG. 8. Vorticity terms (s^{-2}) from the quasigeostrophic model for continuously sheared mean flow limit: (a) vertical section of advection of relative vorticity term and (b) vertical structure of all vorticity terms including advection of relative vorticity $\mathbf{u} \cdot \nabla\zeta$, stretching $-f(\partial w/\partial z)$, and advection of planetary vorticity βv.

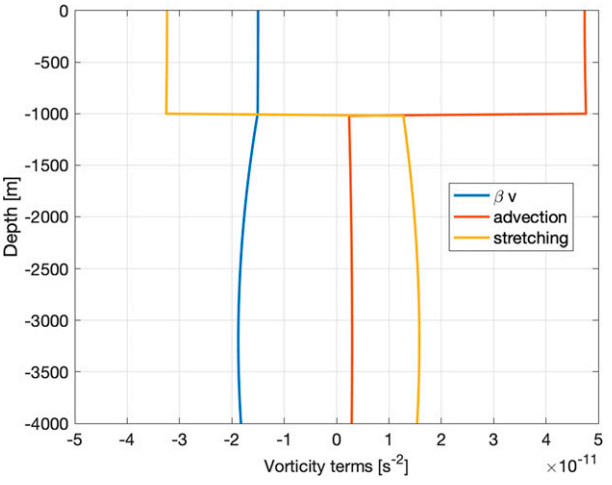

FIG. 9. Vertical structure of vorticity terms (s^{-2}) including advection of relative vorticity $\mathbf{u} \cdot \nabla\zeta$, stretching $-f(\partial w/\partial z)$, and advection of planetary vorticity βv from the quasigeostrophic model for a step function change in mean flow.

the flow-topography interaction leads to the standing meander signal in the upper ocean seen in the regional model.

1) CONTINUOUS FLOW PROFILE

We generate a sheared mean flow profile as a function of both surface U_s and bottom speeds U_b as follows

$$\overline{u}(z) = (U_s - U_b)\frac{1 - e^{(z+H)/\delta}}{1 - e^{H/\delta}} + U_b, \tag{24}$$

where δ is the vertical decay scale and H is ocean depth. For typical Southern Ocean values of $U_b = 1$ cm s^{-1}, $U_s = 30$ cm s^{-1}, $\delta = 1$ km, and $H = 4$ km the mean flow velocity profile (Fig. 5) results in a regime transition from a wave radiating ($\Lambda^2 > 0$) regime in the deep ocean, where $\beta \gg k^2 U_b$, to an evanescent regime ($\Lambda^2 < 0$) in the upper ocean, where $\beta \ll k^2 U_s$. The horizontal and vertical distribution of the vorticity terms obtained numerically are shown in Fig. 8. We can see that the vorticity balance is different in the deep and upper ocean. In the deep ocean, the vorticity balance is dominated by the advection of planetary vorticity with the other two vorticity terms adding up to balance it, as in the uniform mean flow over large-scale topography limit discussed in section 3c. In contrast, the upper-ocean vorticity balance is dominated by the advection of relative vorticity and stretching terms, with the advection of planetary vorticity playing a minor role, as in the uniform mean flow over small-scale topography limit above. With the parameter Λ^2 changing sign in the interior, the dynamics and corresponding vorticity balance transition continuously from one regime to another within the water column. The advection of relative vorticity and stretching terms are amplified in the upper ocean consistent with their linear scaling on the mean flow $\overline{u}$, while the advection of planetary vorticity remains nearly barotropic throughout the water column. The vertical structure and amplitudes of the QG solution are consistent with the model results for large-scale meander signal in the upper ocean in Figs. 3 and 4.

2) STEP FUNCTION FLOW PROFILE

To further explore the underlying dynamics and the dependence of the solution on the problem parameters, we now consider a step function mean flow profile (Fig. 5) consistent with the continuous mean flow profile in (24). We choose a mean flow $\overline{u} = U_b = 1$ cm s^{-1} in the deep ocean, defined as $z < -1$ km, and referred to as the *bottom layer*. And we set $\overline{u} = U_s = 20$ cm s^{-1} in the upper ocean, defined as $z > -1$ km, and referred to as the *surface layer*. We use the bottom velocity value, 1 cm s^{-1}, rather than the bottom-layer-averaged velocity value because, in linear QG theory, it is the mean flow at the bottom that interacts with topography via the linearized bottom boundary condition. Keeping the same bottom velocity for all mean flow profiles allows us to consider Rossby waves with the same amplitudes and vertical scales generated at the bottom and thus focus on the impact of the mean flow shear aloft (i.e., different profiles) on the Rossby wave propagation. With this step function velocity profile, parameter Λ^2 changes sign at the interface between the two layers with $\Lambda^2 > 0$ (wave radiating regime) in the bottom layer and $\Lambda^2 < 0$ (evanescent regime) in the surface layer. To obtain a full analytical solution, we first find the two solutions for the surface and bottom layers satisfying the surface and bottom boundary conditions in (12) and (13), respectively. Then, we impose additional matching conditions for the vertical structure ϕ and vertical velocity w' of a perturbation at the interface. A full derivation of the solution is given in the appendix. The analytical solutions for the step function mean flow profile are plotted in Fig. 9. The vorticity balance in the bottom and surface layers are quantitatively and qualitatively consistent with the corresponding continuous mean flow solution in Fig. 8, showing a step function amplification of the advection of relative vorticity and stretching terms in the upper ocean and a nearly barotropic advection of planetary vorticity term.

To focus on the meander signal in the upper ocean, we consider the analytical solution in the surface layer $\phi^s(z)$ (see appendix) given by

$$\phi^s(z) = -\alpha \frac{N^2 h_0}{f_0 |\Lambda_b|} \frac{\cosh(|\Lambda_s| z)}{\sin(|\Lambda_b| H_b)}, \tag{25}$$

where Λ_b is the Rossby wave vertical wavenumber in the bottom layer, Λ_s is the imaginary part of Λ in the surface layer, $H_b = 0.75H$ is the thickness of the bottom layer ($H_s = 0.25H$ is the corresponding thickness of the surface layer), and α is a nondimensional factor describing the modulation of the Rossby wave generated in the bottom layer by the dynamics of the surface layer defined as follows

$$\alpha = \left[\cosh(|\Lambda_s| H_s) - \frac{U_s}{U_b} \frac{|\Lambda_s|}{|\Lambda_b|} \cot(|\Lambda_b| H_b) \sinh(|\Lambda_s| H_s) \right]^{-1}. \tag{26}$$

We can see that the surface layer analytical solution in (25) obtained for the step function mean flow profile is a combination of the wave radiating and decaying solutions discussed above. Specifically, the amplitude of the solution has a similar form to the Rossby wave amplitude in the uniform mean flow over large-scale topography limit, while the vertical structure decays exponentially as in the small-scale topography limit discussed above. Although it is a vertically decaying solution, the decay scale $|\Lambda_s|^{-1} = |f_0|/Nk \approx 30$ km is much larger than the vertical scale of the surface layer and hence the decay is insignificant. The decay scale is very large in this limit because the perturbation is generated by the large-scale, hence small wavenumber k, topography.

Assuming that $|\Lambda_s| H_s \ll 1$ and $|\Lambda_b| H_b \ll 1$ and using a Taylor expansion as before, the solution in (25) can be further simplified to the following:

$$\phi^s(z) \approx -\frac{f_0 h_0 U_b}{\beta H_b} \left(1 - \frac{1}{3} \frac{U_s \Lambda_s^2}{U_b \Lambda_b^2} \right)^{-1} \cosh(|\Lambda_s| z). \tag{27}$$

As in the uniform mean flow over large-scale topography limit [Eqs. (21) and (22)], the amplitude of the surface layer solution depends on the bottom layer velocity U_b. To leading order, it scales linearly with the bottom velocity (and with the amplitude of topography) consistent with the generation of perturbations by the bottom flow over topography. The amplitude is also scaled by the factor α, which depends on both bottom and surface layer velocities and represents the interaction between the two layers leading to the modification of the bottom generated Rossby wave signal in the upper ocean.

Based on this analytical solution, we propose the following governing mechanism leading to meander formation in the upper ocean. In the bottom layer, the bottom mean flow U_b interacts with the large-scale topography in the wave radiating regime ($\Lambda^2 > 0$) and leads to the generation of a radiating Rossby wave with the advection of planetary vorticity playing a leading order role. The Rossby wave propagates upward and induces vertical velocity at the interface between the surface and bottom layers. This vertical velocity sets the bottom boundary condition for the dynamics in the surface layer, which stretches or squashes depending on the sign of the vertical velocity. Given that $\Lambda^2 < 0$ in the surface layer, the stretching of the water column is balanced by the advection of relative vorticity with the advection of planetary vorticity now playing a minor role. The surface layer response can also feedback on the bottom layer solution through the vertical velocity at the interface, ultimately leading to a stationary flow response throughout the entire water column that depends on both the surface and bottom velocities. Thus, our theoretical results show that while the meander dynamics in the surface layer is inertial, that is, dominated by the advection of relative vorticity, it is "slaved" to the planetary Rossby wave dynamics in the bottom layer. We hypothesize that the results obtained using a continuously sheared mean flow profile, and the regional model results shown in Fig. 3, represent the same physics.

Our results show that the perturbations in the upper ocean, and the corresponding vorticity balance, are controlled by interaction of the bottom flow with topography. The primary consequence of shear in the mean flow is to amplify bottom-generated perturbations in the upper ocean, creating a regime transition in the vorticity balance between the deep and upper ocean. This implies that changes in the meander curvature, the flexing of the meander as referred to in TNG14, may be a response to changes in the bottom flow. We explore the response of the ACC meanders to the wind in the context of this theory in the next section.

4. Wind sensitivity

ACC meanders are generated by mean flows interacting with midocean ridges. Changes in the wind lead to changes in the ACC mean flow, which in turn are expected to drive the meander response (TNG14). The theory presented above describes how meander characteristics in the upper ocean, for example, advection of relative vorticity, depend on a range of parameters, including the bottom flow. In this section, we test our theory and hence focus on the relationship between the ACC mean flow and the meander characteristics in response to changes in wind. First, we analyze the wind perturbation experiments in our idealized simulations, which allows us to explore the meander response to a wide range of wind amplitudes in fully equilibrated states. Then, we extend our results to the variability of the meander in our regional simulation forced by a seasonally varying forcing. Our focus here is on the meander response; the dynamics that govern the response of the mean ACC flow to wind is outside the scope of this study.

a. *Idealized model*

Results from a series of perturbation experiments with varying wind stress in the idealized model is shown in Figs. 10–12. To characterize the zonal mean flow, we diagnose zonal transports

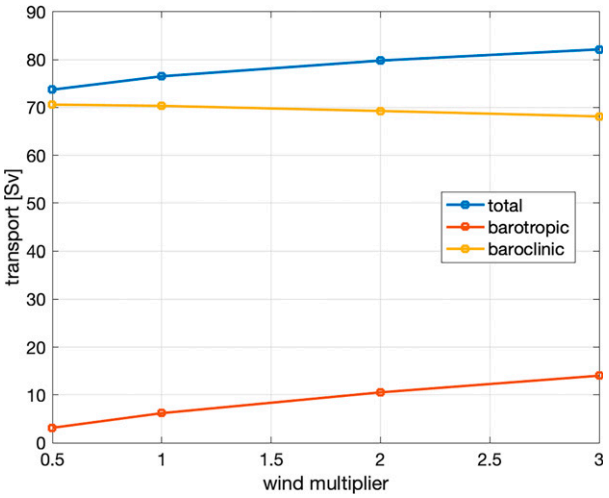

FIG. 10. Transport (Sv) as a function of wind stress in idealized model.

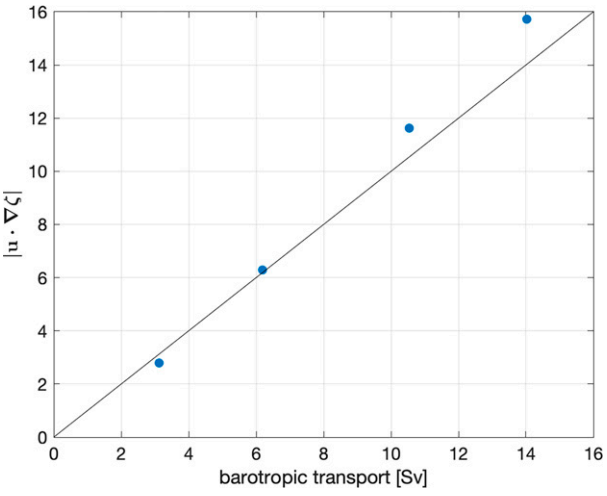

FIG. 12. Dependence of advection of relative vorticity (10^{-8} s^{-2}) on barotropic transport (Sv) in idealized model. Linear dependence (black line) is added.

from the model. Barotropic, baroclinic and total transports are calculated for a section upstream of the ridge to represent the mean flow that interacts with the ridge and leads to the generation of the meander (Fig. 10). We define the barotropic transport as the bottom velocity times the ocean's depth and hence changes in the barotropic transport represent changes in the bottom flow in response to the wind. The baroclinic transport is then computed by subtracting the barotropic transport from the total transport. The baroclinic transport represents the sheared mean ACC flow and its magnitude is dominated by the surface flow. The results show that while the barotropic transport is small, 5%–10% of the total, it scales nearly linearly with the wind. On the other hand, the baroclinic transport dominates the total, but it is relatively insensitive to the wind, that is, it remains saturated. This result is consistent with previous modeling studies showing the saturation of the baroclinic transport of the ACC (e.g., Straub 1993; Munday et al. 2013).

To characterize the response of the meander to the wind, we estimate the absolute value of the advection of relative vorticity at 250-m depth averaged over the meander region and SSH contour length as a proxy for meander flexing (Fig. 11). Both quantities increase under increasing wind, also in agreement with the results of TNG14. However, given that the baroclinic transport (and hence the surface flow) is saturated—isopycnals are also found to be relatively invariant (not shown)—this suggests that the meander characteristics in the upper ocean respond to change in the bottom flow. A relationship between the advection of relative vorticity in the upper ocean and bottom flow in the model is plotted in Fig. 12. It shows a linear dependence, consistent with the mechanism described in the previous section and the analytical solution in (27). The results from the idealized model confirm that, while there is a strong shear in the mean flow and the baroclinic transport accounts for 90% of the total transport, the baroclinic transport is saturated. Changes in the bottom flow (barotropic transport) drive the response of the standing meander in upper ocean.

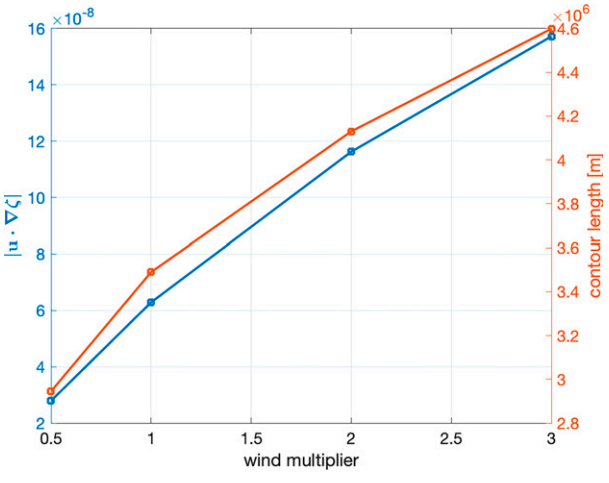

FIG. 11. Meander contour length (m; red line) and advection of relative vorticity (s^{-2}) at 250 m (blue line) as a function of wind stress in the idealized model.

b. *Regional model*

We now explore how the Macquarie Meander simulated by the regional model responds to variability in the wind. The wind stress that forces the regional model represents only the local component of the wind, while the mean ACC flow includes the effect of remote wind forcing, that is, acting outside the domain of the regional model, and applied through the open boundaries. Hence, as above, we explore how changes in the ACC mean flow are related to corresponding changes in the characteristics of the standing meander. We use the monthly mean zonal velocity at the western boundary (our model open boundary condition) to characterize the ACC

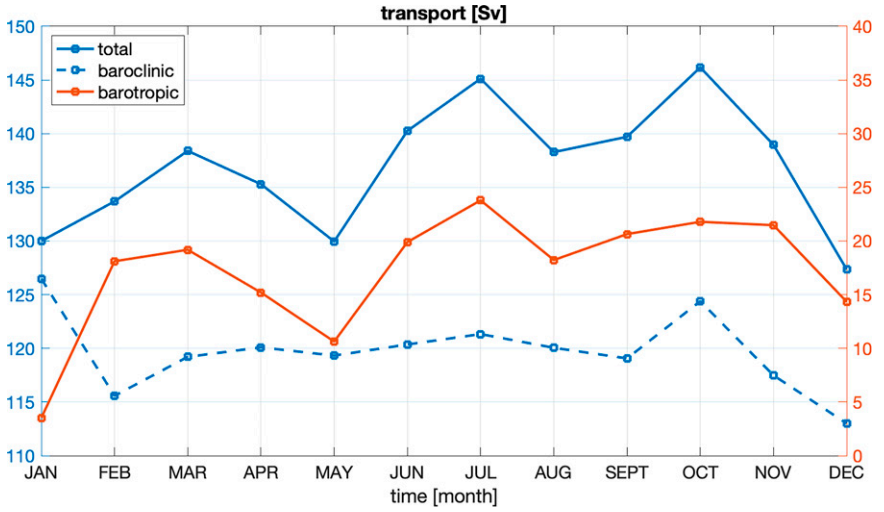

FIG. 13. Time series of inflow transport (Sv) and its barotropic and baroclinic components at western boundary.

mean flow upstream of the Southeast Indian Ridge. The regional model is forced by seasonal repeat-year forcing and hence does not capture the fully equilibrated response of the flow to a long-term change in the wind, as was done using the idealized model above. Nevertheless, there are significant seasonal variations in the wind, and thus in the mean ACC flow, which drive corresponding changes in the standing meander, as we will show below.

Annual variations of the total, barotropic and baroclinic transports of the ACC estimated at the western boundary of the region are plotted in Fig. 13. As before, the barotropic transport is computed by depth-integrating the bottom velocity and hence represents the variability of the bottom flow within this region. Barotropic transport is highly correlated with total transport (correlation coefficient = 0.81), while the correlation between total transport and baroclinic component is around 0.37. The results show that, although the barotropic transport contributes much less (about 10%) than the baroclinic transport (about 90%) to the total time-mean ACC transport, it dominates the variability of the total ACC transport. While the baroclinic transport varies in the range 115–125 Sv (1 Sv $\equiv 10^6$ m^3 s^{-1}) and hence changes by about 10%, the barotropic transport varies in the range 10–25 Sv and hence changes by as much as 100%.

We select *weak* (January) and *strong* (July) mean ACC flow periods based on the strength of the total transport at the western boundary. To filter out variability associated with transient eddies in the model, we average meander characteristics over these two periods and also composite-average them over the 4 years of the simulation. The mean SSH contours for the weak and strong mean flow periods are shown in Fig. 14. The meander contours become longer (the length of

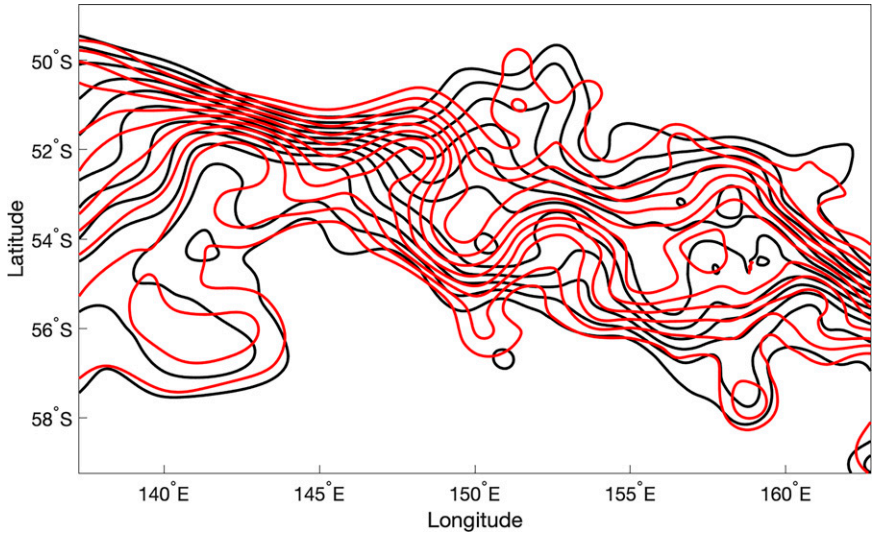

FIG. 14. Sea surface height (m) contours for weak current (black) and strong current (red) period. From south to north are contours from −0.5 to 0.5 m with 0.1-m interval.

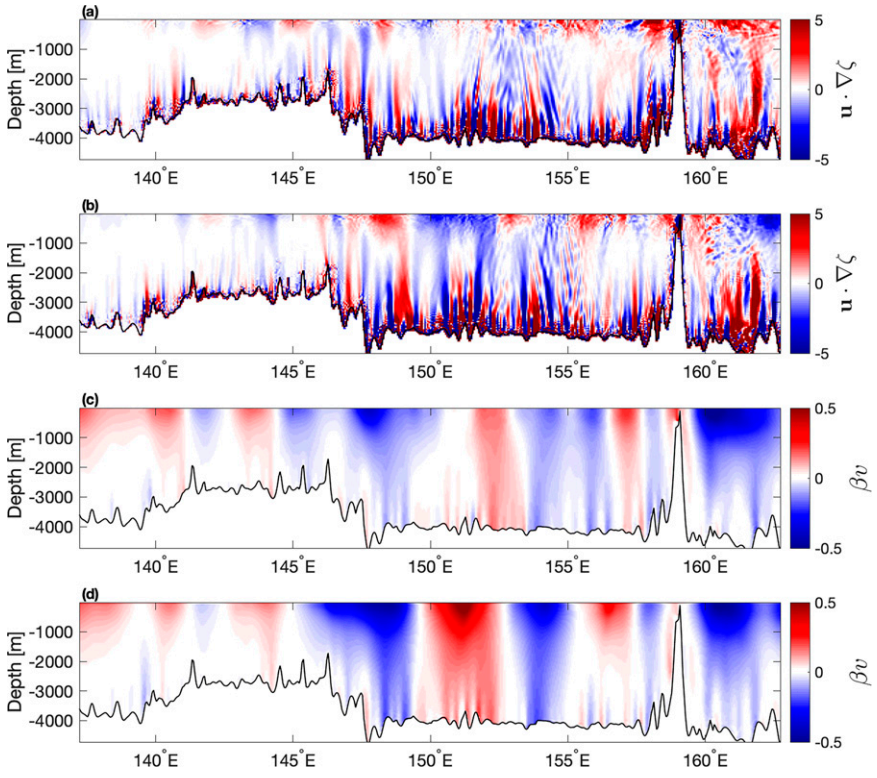

FIG. 15. Vorticity sections at 54°S of advection of relative vorticity $\mathbf{u} \cdot \nabla\zeta$ and advection of planetary vorticity βv for the (a),(c) weak current and (b),(d) strong current period.

SSH contours between −0.5 and 0.5 m increases by around 200 km) and more "flexed" in the strong mean flow period, consistent with the modeling results of TNG14. However, the baroclinic transport, and hence the upper-ocean ACC flow, changes very little between the two periods, suggesting that the meander response is driven by changes in the bottom (barotropic) flow. To demonstrate this more quantitatively, we show the corresponding changes in the advection of relative and planetary vorticity at 54°S in Fig. 15. The results show that while there is a similar overall structure of the meander between the two periods, the amplitude of the advection of relative vorticity (and of the stretching term balancing it) increases by up to a factor of 2 in the strong mean flow period, consistent with the corresponding changes in the bottom flow.

5. Discussion and conclusions

Standing meanders contribute to the meridional heat and vertical momentum transfers in the Southern Ocean and play an important role for the equilibration of the ACC. The flexing of standing meanders, which implies a change in the vorticity balance, has been suggested to facilitate the transfer of the momentum input by the wind to the ocean seafloor and thus to control the response of the ACC to wind. However, the underlying dynamics governing the adjustment of the meander vorticity balance and its response to the wind remain unclear. In this study, we explore the formation and vorticity dynamics of a standing meander using numerical models and theory.

Our results show that the meander structure throughout the entire water column is set by a stationary Rossby wave generated from the interaction between the bottom flow and large-scale topography. In the deep ocean, where the mean ACC flow is weak, the vorticity balance is dominated by the advection of planetary vorticity and stretching, leading to the generation of a radiating Rossby wave. The vertical shear of the mean ACC flow creates a regime transition and a change in the dominant vorticity balance within the water column. In the upper ocean, where mean ACC flow is large, stretching resulting from the bottom generated Rossby wave is balanced by the advection of relative vorticity, with the advection of planetary vorticity playing a minor role. Thus, the vorticity balance in the upper ocean—diagnosed in our regional and idealized models, and previously in a global ocean model (TNG14)—is slaved to the planetary vorticity balance in the deep ocean and maintained by the bottom flow interacting with large-scale topography. Consistently, the analytical solution derived in the limit of a step function mean flow profile (25) shows that, to the leading order, the upper-ocean meander signal scales linearly with the magnitude of the bottom flow and the horizontal scale of the topography.

The dependence of the upper-ocean meander signal on the bottom flow suggests a novel mechanism for the response of the ACC meanders to wind. The existing framework for the

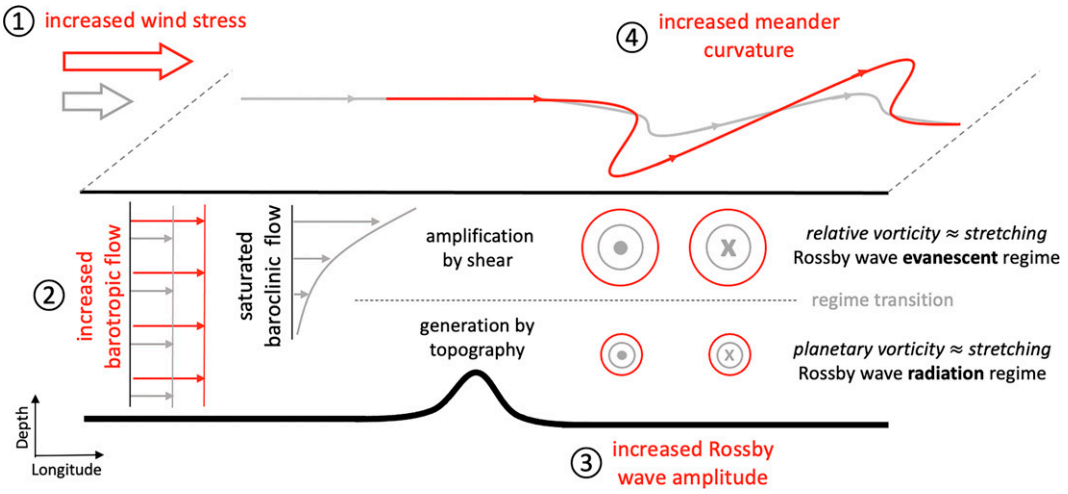

FIG. 16. A schematic illustrating the adjustment of a standing meander to an increase in the wind stress. Red curves and text display the response to the increased wind stress while solid gray curves represent the reference state. An increase in the surface wind increases the bottom (barotropic) flow. The stronger bottom flow interacts with large-scale topography and generates a Rossby wave. The baroclinic flow aloft remains constant (saturated) with the wind increase. In turn, the mean ACC shear amplifies the Rossby wave and leads to a regime transition in the water column with an increase in the amplitude of the captured Rossby wave and thus the curvature of the standing meander.

adjustment of a standing meander to changes in wind proposed in TNG14 invokes *baroclinic* processes. In the TNG14 framework, stronger wind acts to steepen isopycnals upstream of a ridge and thus leads to a stronger mean (baroclinic) ACC flow in the upper ocean. In turn, stronger mean ACC flow arrests a different wavenumber Rossby wave, leading therefore to a change in the standing meander shape (or curvature) referred to as flexing of the meander. Flexing of the meander has been suggested to lead to the enhancement of transient eddies and their fluxes, and thus a relaxation of isopycnals within the meander region downstream of the ridge (e.g., Abernathey and Cessi 2014).

Based on our results, we propose an alternative mechanism for the response of ACC meanders to changes in wind forcing (Fig. 16). Stronger wind leads to stronger bottom (barotropic) flow. Interaction of stronger bottom flow with topography generates a larger-amplitude Rossby wave and meander. As this larger-amplitude Rossby wave propagates into the upper ocean where inertial terms are large, advection of relative vorticity and stretching increase and dominate the vorticity balance. Therefore, the amplitude of the standing meander increases in response to the increase in bottom flow driven by stronger wind forcing, leading to flexing of the meander and an increase in the curvature (contour length). An increase in the bottom flow is also expected in order for topographic form stress to balance the increased wind stress (e.g., Masich et al. 2015)—dynamics not discussed in this study.

The mechanism proposed here can be described as a bottom-up control of the response of the ACC to wind, in contrast to the top-down mechanism proposed in TNG14. The major difference between the two mechanisms is whether the barotropic or baroclinic component of the mean ACC flow responds to the wind. Consistent with previous studies suggesting saturation of the ACC, our modeling results show that while the bottom (barotropic) flow increases under increasing wind, the baroclinic flow component is insensitive to changes in wind. The baroclinic flow does, however, have a strong influence on the vorticity balance of the meander, as it is the strong baroclinic shear that is responsible for the regime change within the water column. Our study suggests that interaction of the barotropic flow with topography sets the characteristics of standing meanders in the ACC, which in turn regulate the response of the ACC as a whole to changes in wind forcing.

Acknowledgments. This work was supported in part by funding from the Australian Government as part of the Antarctic Science Collaboration Initiative program, through the Australian Antarctic Program Partnership, and from the Centre for Southern Hemisphere Oceans Research, a partnership between CSIRO, the Qingdao National Laboratory for Marine Science and Technology, the University of Tasmania, and the University of New South Wales. This research was undertaken on the NCI National Facility in Canberra, Australia. The authors thank two anonymous reviewers for their constructive comments.

Data availability statement. Datasets analyzed during the current study are available at https://github.com/XihanZh/standing_meander_vorticity.

APPENDIX

Analytical Solution in the Case of a Step Function Mean Flow Profile

To find a complete solution in the case of a step function mean flow profile, we find solutions in the surface and bottom layers satisfying the bottom and surface boundary conditions,

respectively. Then, we also impose a matching condition at the interface at 1-km depth ($z^* = -H/4$).

In the surface layer, $\Lambda^2 < 0$ and hence a general solution to the governing QG equation can be written in the form

$$\phi^s(z) = A\exp(|\Lambda_s|z) + B\exp(-|\Lambda_s|z), \tag{A1}$$

where A and B are coefficients and Λ_s is imaginary part of Λ in the surface layer. In the bottom layer, $\Lambda^2 > 0$ and the corresponding solution is written as

$$\phi^b(z) = C\sin[|\Lambda_b|(z + H)] + D\cos[|\Lambda_b|(z + H)], \tag{A2}$$

where Λ_b is the real part of Λ in the bottom layer—a wave vertical wavenumber. We impose two boundary conditions, one at the surface and one at the bottom, as in the uniform mean flow cases above. In addition, we also impose two matching conditions at the interface depth z^*: one for the vertical structure function ϕ and the other for the vertical velocity w'. All boundary and matching conditions are

$$\phi^s_z(0) = 0, \tag{A3}$$

$$\phi^b_z(-H) = -\frac{N^2h_0}{f_0}, \tag{A4}$$

$$\phi^s(z^*) = \phi^b(z^*), \quad \text{and} \tag{A5}$$

$$U_s\phi^s_z(z^*) = U_b\phi^b_z(z^*). \tag{A6}$$

These four conditions complete the problem and allow us to determine four unknown coefficients of the surface and bottom layer solutions. Applying the boundary conditions to the corresponding solutions above, we get

$$A = B, \tag{A7}$$

$$C = -\frac{N^2h_0}{f_0|\Lambda_b|}, \tag{A8}$$

$$2A\cosh\left(|\Lambda_s|\frac{H}{4}\right) = C\sin\left(|\Lambda_b|\frac{3H}{4}\right) + D\cos\left(|\Lambda_b|\frac{3H}{4}\right), \quad \text{and} \tag{A9}$$

$$-2U_sA|\Lambda_s|\sinh\left(|\Lambda_s|\frac{H}{4}\right) = U_bC|\Lambda_b|\cos\left(|\Lambda_b|\frac{3H}{4}\right) - U_bD|\Lambda_b|\sin\left(|\Lambda_b|\frac{3H}{4}\right). \tag{A10}$$

From here, each of the unknown coefficients can be written as

$$C = -\frac{N^2h_0}{f_0|\Lambda_b|}, \tag{A11}$$

$$A = \frac{C}{2}\left[\sin(|\Lambda_b|H_b)\cosh(|\Lambda_s|H_s) - \frac{U_s}{U_b}\frac{|\Lambda_s|}{|\Lambda_b|}\cos(|\Lambda_b|H_b)\sinh(|\Lambda_s|H_s)\right]^{-1}, \quad \text{and} \tag{A12}$$

$$D = 2A\left[\cos(|\Lambda_b|H_b)\cosh(|\Lambda_s|H_s) + \frac{U_s}{U_b}\frac{|\Lambda_s|}{|\Lambda_b|}\sin(|\Lambda_b|H_b)\sinh(|\Lambda_s|H_s)\right], \tag{A13}$$

where $H_b = 0.75H$ is the thickness of the bottom layer and $H_s = 0.25H$ is the corresponding thickness of the surface layer.

All coefficients are now written in terms of the problem parameters and determine a complete solution to the QG governing equation that satisfies the top and bottom boundary conditions. The condition $A = B$ above implies that the solution for the vertical structure in the surface layers reduces to

$$\phi^s(z) = A\cosh(|\Lambda_s|z), \tag{A14}$$

with the amplitude A given in terms of the problem parameters as

$$A = -\frac{N^2h_0}{f_0|\Lambda_b|}\left[\sin(|\Lambda_b|H_b)\cosh(|\Lambda_s|H_s) - \frac{U_s}{U_b}\frac{|\Lambda_s|}{|\Lambda_b|}\cos(|\Lambda_b|H_b)\sinh(|\Lambda_s|H_s)\right]^{-1}. \tag{A15}$$

REFERENCES

Abernathey, R., and P. Cessi, 2014: Topographic enhancement of eddy efficiency in baroclinic equilibration. *J. Phys. Oceanogr.*, **44**, 2107–2126, https://doi.org/10.1175/JPO-D-14-0014.1.

——, J. Marshall, and D. Ferreira, 2011: The dependence of Southern Ocean meridional overturning on wind stress. *J. Phys. Oceanogr.*, **41**, 2261–2278, https://doi.org/10.1175/JPO-D-11-023.1.

Becker, J., and Coauthors, 2009: Global bathymetry and elevation data at 30 arc seconds resolution: SRTM30_PLUS. *Mar. Geod.*, **32**, 355–371, https://doi.org/10.1080/01490410903297766.

Chereskin, T., L. Talley, and B. Sloyan, 2010: Nonlinear vorticity balance of the Subantarctic Front in the southeast Pacific. *J. Geophys. Res.*, **115**, C06026, https://doi.org/10.1029/2009JC005611.

Constantinou, N. C., 2018: A barotropic model of eddy saturation. *J. Phys. Oceanogr.*, **48**, 397–411, https://doi.org/10.1175/JPO-D-17-0182.1.

——, and W. R. Young, 2017: Beta-plane turbulence above monoscale topography. *J. Fluid Mech.*, **827**, 415–447, https://doi.org/10.1017/jfm.2017.482.

——, and A. M. Hogg, 2019: Eddy saturation of the Southern Ocean: A baroclinic versus barotropic perspective. *Geophys. Res. Lett.*, **46**, 12 202–12 212, https://doi.org/10.1029/2019GL084117.

Dufour, C. O., J. Le Sommer, J. D. Zika, M. Gehlen, J. C. Orr, P. Mathiot, and B. Barnier, 2012: Standing and transient eddies in the response of the Southern Ocean meridional overturning to the southern annular mode. *J. Climate*, **25**, 6958–6974, https://doi.org/10.1175/JCLI-D-11-00309.1.

Farneti, R., and Coauthors, 2015: An assessment of Antarctic Circumpolar Current and Southern Ocean meridional overturning

circulation during 1958–2007 in a suite of interannual CORE-II simulations. *Ocean Modell.*, **93**, 84–120, https://doi.org/10.1016/j.ocemod.2015.07.009.

Gill, A. E., 1982: *Atmosphere–Ocean Dynamics*. Academic Press, 662 pp.

Hallberg, R., and A. Gnanadesikan, 2006: The role of eddies in determining the structure and response of the wind-driven Southern Hemisphere overturning: Results from the Modeling Eddies in the Southern Ocean (MESO) project. *J. Phys. Oceanogr.*, **36**, 2232–2252, https://doi.org/10.1175/JPO2980.1.

Hughes, C. W., 2005: Nonlinear vorticity balance of the Antarctic Circumpolar Current. *J. Geophys. Res.*, **110**, C11008, https://doi.org/10.1029/2004JC002753.

Johnson, E. R., 1977: Stratified Taylor columns on a beta-plane. *Geophys. Astrophys. Fluid Dyn.*, **9**, 159–177, https://doi.org/10.1080/03091927708242323.

Kiss, A. E., and Coauthors, 2020: ACCESS-OM2 v1. 0: A global ocean–sea ice model at three resolutions. *Geosci. Model Dev.*, **13**, 401–442, https://doi.org/10.5194/gmd-13-401-2020.

Marshall, D. P., M. H. Ambaum, J. R. Maddison, D. R. Munday, and L. Novak, 2017: Eddy saturation and frictional control of the Antarctic Circumpolar Current. *Geophys. Res. Lett.*, **44**, 286–292, https://doi.org/10.1002/2016GL071702.

Marshall, J., and T. Radko, 2003: Residual-mean solutions for the Antarctic Circumpolar Current and its associated overturning circulation. *J. Phys. Oceanogr.*, **33**, 2341–2354, https://doi.org/10.1175/1520-0485(2003)033<2341:RSFTAC>2.0.CO;2.

——, and K. Speer, 2012: Closure of the meridional overturning circulation through Southern Ocean upwelling. *Nat. Geosci.*, **5**, 171–180, https://doi.org/10.1038/ngeo1391.

——, A. Adcroft, C. Hill, L. Perelman, and C. Heisey, 1997: A finite-volume, incompressible Navier Stokes model for studies of the ocean on parallel computers. *J. Geophys. Res.* **102**, 5753–5766, https://doi.org/10.1029/96JC02775.

Masich, J., T. K. Chereskin, and M. R. Mazloff, 2015: Topographic form stress in the Southern Ocean state estimate. *J. Geophys. Res. Oceans*, **120**, 7919–7933, https://doi.org/10.1002/2015JC011143.

Meredith, M. P., and A. M. Hogg, 2006: Circumpolar response of Southern Ocean eddy activity to a change in the Southern Annular Mode. *Geophys. Res. Lett.*, **33**, L16608, https://doi.org/10.1029/2006GL026499.

Munday, D. R., H. L. Johnson, and D. P. Marshall, 2013: Eddy saturation of equilibrated circumpolar currents. *J. Phys. Oceanogr.*, **43**, 507–532, https://doi.org/10.1175/JPO-D-12-095.1.

Rintoul, S. R., and A. C. N. Garabato, 2013: Dynamics of the Southern Ocean circulation. *Ocean Circulation and Climate: A 21st Century Perspective*, G. Siedler et al., Eds., International Geophysics Series, Vol. 103, Elsevier, 471–492.

Salmon, R., 1998: *Lectures on Geophysical Fluid Dynamics*. Oxford University Press, 378 pp.

Sandwell, D. T., and W. H. Smith, 2009: Global marine gravity from retracked Geosat and ERS-1 altimetry: Ridge segmentation versus spreading rate. *J. Geophys. Res.*, **114**, 2008JB006008, https://doi.org/10.1029/2008JB006008.

Straub, D. N., 1993: On the transport and angular momentum balance of channel models of the Antarctic Circumpolar Current. *J. Phys. Oceanogr.*, **23**, 776–782, https://doi.org/10.1175/1520-0485(1993)023<0776:OTTAAM>2.0.CO;2.

Thompson, A. F., and A. C. Naveira Garabato, 2014: Equilibration of the Antarctic Circumpolar Current by standing meanders. *J. Phys. Oceanogr.*, **44**, 1811–1828, https://doi.org/10.1175/JPO-D-13-0163.1.

Vallis, G. K., 2019: *Essentials of Atmospheric and Oceanic Dynamics*. Cambridge University Press, 366 pp.

Williams, R. G., C. Wilson, and C. W. Hughes, 2007: Ocean and atmosphere storm tracks: The role of eddy vorticity forcing. *J. Phys. Oceanogr.*, **37**, 2267–2289, https://doi.org/10.1175/JPO3120.1.

Zhang, X., and M. Nikurashin, 2020: Small-scale topographic form stress and local dynamics of the Southern Ocean. *J. Geophys. Res. Oceans*, **125**, e2019JC015420, https://doi.org/10.1029/2019JC015420.